This is a post-print. Please check (and cite 😊) the accepted version at:

ACS applied materials & interfaces 13 (30), 36416-36425 (2021)

DOI: /10.1021/acsami.1c06204

The SI is attached at the end of this file.

SI videos are available at:

https://hagayshpaisman.wixsite.com/shpaismanlab/copy-of-videos

Laser printing of multi-layered alternately conducting and insulating micro-structures

Eitan Edri,[1,2] *Nina Armon,*[1,2] *Ehud Greenberg,*[1,2] *Shlomit Moshe-Tsurel,*[1,2] *Danielle Lubotzky,*[1,2] *Tommaso Salzillo,*[3] *Ilana Perelshtein,*[2] *Maria Tkachev,*[2] *Olga Girshevitz*[2] *and Hagay Shpaisman*,*[1,2]

[1] Department of Chemistry, Bar-Ilan University, Ramat Gan 5290002, Israel

[2] Institute for Nanotechnology and Advanced Materials (BINA), Bar-Ilan University, Ramat Gan 5290002, Israel

[3] Department of Chemical and Biological Physics, Weizmann Institute of Science, Rehovot 76100, Israel

KEYWORDS: multi-layered structures, microbubble, conducting/insulating, pattern formation, microfluidics

ABSTRACT

Production of multi-layered micro-structures composed of conducting and insulating materials is of great interest as they can be utilized as micro-electronic components. Current proposed fabrication methods of these micro-structures include top-down and bottom-up methods, each have its own set of drawbacks. Laser based methods were shown to pattern various materials with micron/sub-micron resolution, however, multi-layered structures demonstrating conducting/insulating/conducting properties were not yet realized.

Here, we demonstrate laser printing of multi-layered micro-structures consisting of platinum conducting and silicon oxide insulating layers by a combination of thermally driven reactions with micro-bubble assisted printing. $PtCl_2$ dissolved in N-methyl-2-pyrrolidone (NMP) was used as a precursor to form conducting Pt layers, while tetraethyl orthosilicate dissolved in NMP formed insulating silicon oxide layers identified by Raman spectroscopy. We demonstrate control over the height of the insulating layer between ~50–250 nm by varying the laser power and number of iterations. The resistivity of the silicon oxide layer at 0.5 V was 1.5×10^{11} Ωm. Other materials

that we studied were found to be porous and prone to cracking, rendering them irrelevant as insulators. Finally, we show how microfluidics can enhance multi-layered laser microprinting by quickly switching between precursors. The concepts presented here could provide new opportunities for simple fabrication of multi-layered micro-electronic devices.

INTRODUCTION

Fabrication of multilayered micro-structures composed of insulating and conducting materials is of great interest, as they are utilized as components in various micro-electronic devices such as capacitors,[1,2] transistors,[3] inductors,[2] light-emitting diodes,[4] and batteries.[4] Other possible applications include printed circuit boards,[5] solar cells,[6] and medical devices.[7] The purpose of the insulating layers is to electrically separate between conductive layers[3] and to optimize the charge balance.[8] In addition, such layers are often deposited for protection, e.g. to avoid oxidation of the conductive layers.[5] The thickness of insulating layers ranges between a few nanometers to several microns.[9,10] Fabrication of conducting/insulating micro-structures is currently performed mostly by photolithography methods,[11–13] which provide layers with controlled and homogenous thickness.[9,14] However, similar to other top-down approaches, these methods require multiple production steps, masks, and expensive fabrication setups, and are considered wasteful in terms of materials and energy consumption. Bottom-up printing methods such as ink-jet,[1,9,14] aerosol-jet[15,16], and screen-printing[4] were used to form micro-structures containing conducting/insulating layers with minimal material waste.[4] Other methods, such as stereolithography[17–19] could be adapted(multiple) to form such structures. However, these methods usually employ polymers or ionic liquids as insulating layers rather than the more stable inorganic oxides, often require

stabilization of the dispersions by undesired additives, and involve post-processing steps.[4] The minimal feature size demonstrated was tens of microns while aerosol and screen printing only provide relatively thick layers (several microns).

Light-matter interactions gained wide attention during recent decades and were shown to promote material deposition. Laser assembly from liquid precursors provides smaller feature size than from powders while allowing relatively simple setups, easy handling, and recycling. Many demonstrations of this approach were presented using a similar basic setup, with a surprising number of underlying mechanisms.[20] These methods can be divided according to the source of the deposited material: preformed or locally synthesized. The study presented in this manuscript utilizes a combination of methods from both approaches: microbubble assisted printing of preformed materials with thermally driven reactions where locally synthesized materials are deposited. Microbubble assisted printing was shown to deposit metals,[21,22] polymers,[23–25] semiconductors[24] and organic molecules,[26] while thermally driven reactions showed depositions of metals,[27–29] oxides,[27,28,30–34] organic molecules,[35] and molecular compounds.[28] Multi-layered structures were demonstrated using thermally driven reactions,[30] but the minimal thickness of several microns per layer renders them unsuitable for many micro-electronic applications. In addition, electron transport studies on oxides were not performed, therefore their relevance for conducting/insulating/conducting micro-structures is not clear. A combination of microbubble assisted printing with thermally driven reactions was demonstrated for assemblies of metals,[36] oxides,[36,37] polymers,[38] metal organic frameworks,[39] and alloys.[40] Experimental studies[36] showed that NPs are formed in the liquid phase and carried to the micro-bubble base where they are deposited along with materials that are locally synthesized at the same location.

Formation of the desired micro-structures is challenging, as the deposition process is relatively aggressive, and the integrity of the underlying layers can be compromised. In addition, pores and cracks in the insulating layer must be avoided while maintaining minimal thickness. After examining various materials as candidates for the insulating layer, we found that tetraethyl orthosilicate (TEOS) can be used to form silicon oxide layers, which can withstand microprinting of additional layers on top of them while maintaining insulating properties. We demonstrate control over the height of the insulating layer between about 50 to 250 nm by increasing the laser power or the number of layers. Moreover, we show that a microfluidic channel can be utilized to quickly switch between media, enabling rapid production of multi-layered micro-structures. These new approaches could therefore provide new opportunities for various applications such as multi-layered micro-electronic devices and micro-capacitors.

RESULTS AND DISCUSSION

A 532 nm continuous wave (CW) laser was focused on the liquid medium (**Figure 1a**) containing the required precursors inserted between two glass slides (**Figure 1b**). $PtCl_2$ dissolved in N-methyl-2-pyrrolidone (NMP) was used to form conducting Pt layers, while TEOS dissolved in NMP containing small amounts of aqueous NaOH was found to form insulating silicon oxide layers by condensation polymerization (**Figure S1**). The microscope stage was computer-controlled, and the experiments were recorded using a CMOS camera. To form patterns, unless otherwise stated, the microscope stage was moved along a predetermined path at 100 µm/s for Pt deposition and 400 µm/s for silicon oxide deposition with laser illuminating power of 14 mW. Laser modulation was used to achieve continuous depositions (see more details in the experimental section).

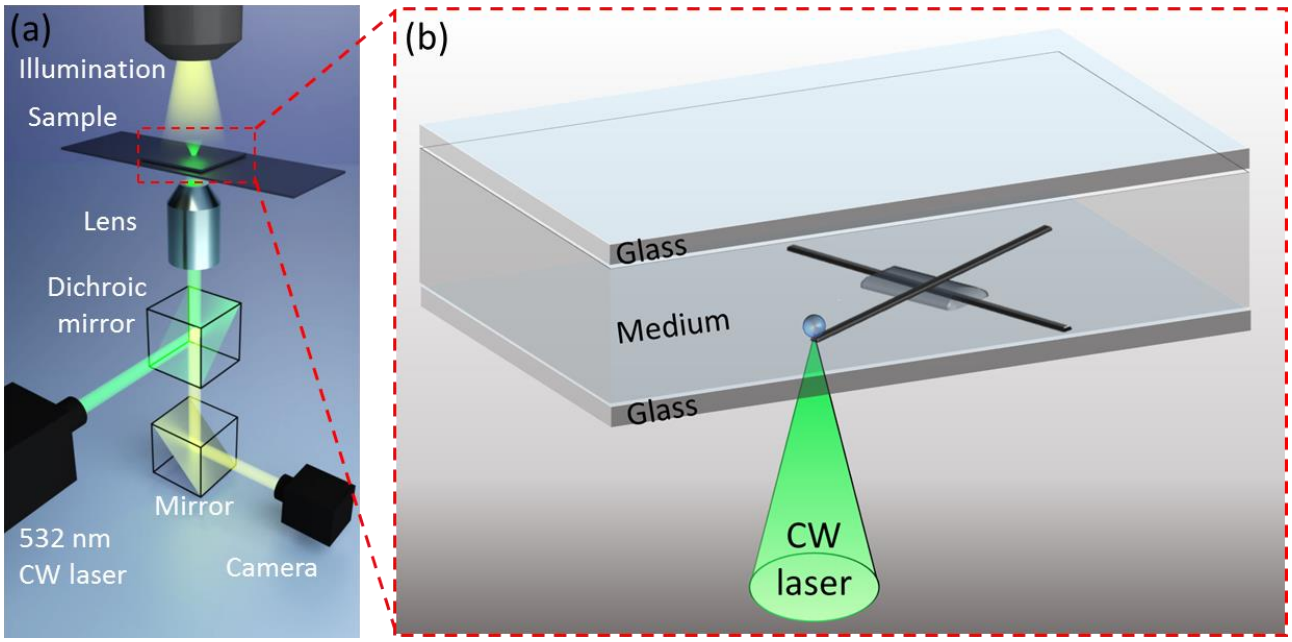

Figure 1. Illustrations of (a) optical setup and (b) sample geometry. Multi-layered micro-patterns are fabricated between two glass slides filled with precursors by moving the microscope stage relative to the sample.

In order to examine the electrical transport properties of the insulating layer, a conducting/insulating/conducting multi-layered micro-structure was formed (**Figure 2**). A cover slide with four sputtered gold pads was used as the substrate. A Pt line (**Figure 2a**) was deposited, connecting two of the gold pads (**Figure 2e**), and an insulating silicon oxide layer was selectively deposited on top of the Pt line only in the area later used to form an electrical junction (**Figure 2b**). To achieve good electrical isolation, three repetitions of the silicon oxide deposition process were performed, and the line was deliberately wider than the underlying Pt line, fully covering even its edges. Finally, another Pt line was printed between two other gold pads, perpendicular to the previously printed lines. This line forms an electrical junction with the silicon oxide in-between the two Pt lines (**Figure 2c-d**). High-resolution scanning electron microscope (HR-SEM) images (**Figure 3a**) show that all three layers seem to be continuous, and that the middle layer fully covers the bottom Pt line. EDS mapping (**Figure 3b-d**) is consistent with the expected chemical elements. The entire process is shown in **Video SV1** in the Supporting Information. A micro-bubble is clearly visualized throughout the printing process. Its role in material deposition is discussed below.

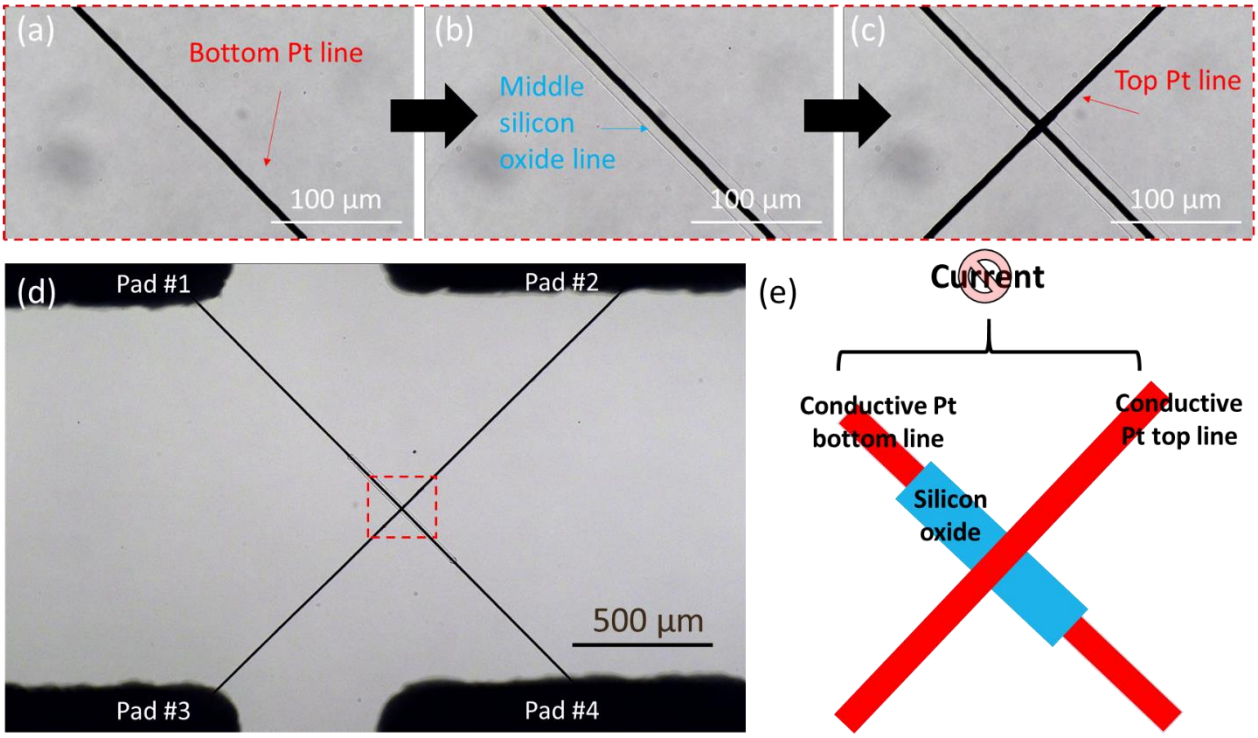

Figure 2. (a-c) Bright-field microscopy images showing the steps for fabricating conducting/insulating/conducting microstructures: (a) Microprinting the bottom Pt conducting line, (b) silicon oxide layer and (c) top Pt line. (d) Bright-field microscopy zoomed out image and (e) Illustration presenting the scheme for electrical measurements.

We performed Raman measurements (**Figure 3e)** that agreed with previously reported spectra of silicon oxides. The peaks at 464 cm^{-1} corresponds to the silane network binding (Si-O-Si stretching-bending),[41,42] while 490 cm^{-1} is associated with vibrational modes of tetracyclosiloxane rings.[43–45] The peak at 804 cm^{-1} corresponds to Si–O antisymmetric stretching[46] or Si-O-Si bending.[47] The large peak at 980 cm^{-1} is assigned to Si-OH stretch vibrations.[45,48] The 464 cm^{-1} peak could be indicative of a crystalline structure as for amorphous silica there is a significantly broader peak around the same location.[42] However, both amorphous and crystalline structures might be present, and a dedicated study should be performed to clarify the crystallinity ratio. There

is no significant signal around 1300-1400 cm^{-1} (D band) typical of carbon-based materials, suggesting that residual carbon is minimal.

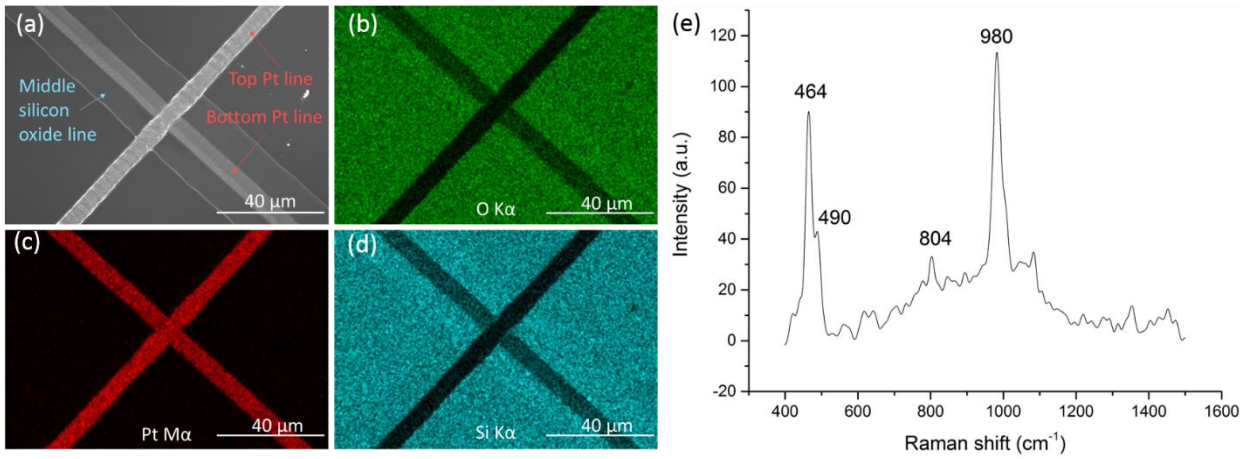

Figure 3. (a) Scanning electron microscope image of fabricated microstructure. (b-d) EDS mapping demonstrating the presence of O, Pt and Si in the appropriate layers. (e) Raman spectrum (using a 785 nm laser) of microprinted silicon oxide layer on gold.

For investigating the sub-micron structure of the fabricated layers, we performed cross sectioning by focused ion beam (FIB). HR-SEM imaging (**Figure 4a,b**) along with EDS mapping of Si and Pt (**Figure 4c,d**) reveal the presence of the three layers. The thickness of the silicon oxide layer is ~170 nm. Moreover, the images show that the relatively aggressive deposition process of the second and third layers did not compromise the integrity of the underlying layers. The insulating layer shows neither pores nor cracks.

Electrical measurements show that the Pt lines are conductive and show resistivity of $3.2 \pm 0.6 \times 10^{-6}$ Ωm. This value is slightly better than previously reported state-of-the-art values for laser based micro-printed Pt ($4.2 \pm 0.5 \times 10^{-6}$ Ωm).[49] In order to characterize the nano-structure of Pt

depositions, TEM lamellas were formed using FIB. As shown in **Figure S2a** the deposits are composed of fused nano-crystals with clear atomic planes. Selected area diffraction pattern (SADP) measurements **(Figure S2b)** show d-spacing associated with face-centered-cubic (fcc) platinum. EDS measurements of Pt lines (**Figure S2c)** didn't show evidence of residual elements (such as Cl or C).

Figure 4e shows typical I-V curves of the three different contact combinations of the layered junction. Measurements along the bottom (pads #1 & #4) and top (pads #2 & #3) Pt lines indicate that both lines are conductive, while measurements between the two lines (pads #1 & #2 or #3 & #4) show high resistance. For evaluating the resistivity of the silicon oxide, a bigger contact area is required. We therefore prepared a layered structure by laser microprinting of silicon oxide on top of gold evaporated on a glass substrate. Silver paste was applied on the silicon oxide layer, achieving an Ag/silicon oxide/gold multi-layered structure (**Figure 4f**). The resistivity of the silicon oxide layer was found to be $1.5 \pm 0.5 \times 10^{11}$ **Ω**m between 0 and 0.5 V. This value is sufficient for various applications, however it is about two orders of magnitude lower than previously reported values for silicon oxide,[50] possibly due to incorporation of precursors in nanopores. In addition, tunneling atomic force microscopy (TUNA) measurements were performed on the thinnest silicon oxide layers that we were able to prepare on an evaporated gold layer (**Figure 4g,h**) by significantly increasing the stage velocity (to 10 mm/sec, the fastest our stage can move). Note that these layers are the only non-continuous ones in this study and are atypical compared to the other layers of silicon oxide that provide uniform coverage. We found regions of silicon oxide as thin as ~10 nm, however even these layers were too insulating to allow quantitative analysis. TUNA measurements showed currents comparable to the background noise, indicating high resistivity of the silicon oxide layers.

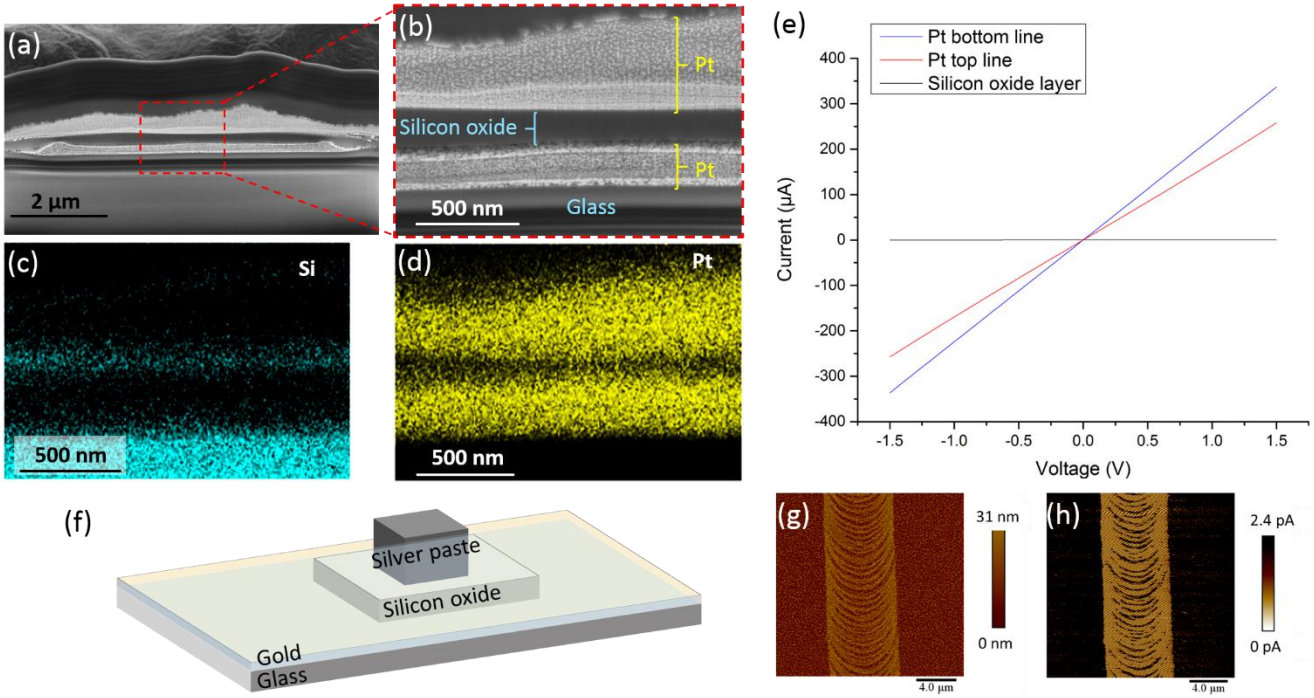

Figure 4. (a,b) HR-SEM images and (c,d) EDS mapping of Si and Pt of FIB cross-sectioned multi-layered micro-structure. (e) Typical I-V curves of the three different contact combinations of the layered junction. Measurements along the bottom (pads #1 & #4) and top (pads #2 & #3) Pt lines indicate that they are conductive, while measurements between the top and bottom lines (pads #1 & #2 or #3 & #4) indicate high resistivity of silicon oxide. (f) Illustration of Ag/silicon oxide/gold multi-layered structure fabricated for evaluating the resistivity of the silicon oxide.(g) Atomic force microscopy topography image and (h) TUNA measurements of thin (down to ~10 nm) silicon oxide layers, yielding currents comparable to the background noise, indicating high resistivity.

Prior to our findings on microprinting of TEOS presented above, we examined various materials that were expected to form suitable insulating layers. A list of the materials is provided in the Supporting Information. While we have not performed an in-depth study on each material, here we shortly hypothesize why they failed to form appropriate insulating deposits. The materials can be divided into two categories: preformed NPs and inorganic metal ion precursors. Deposition of electrically insulating NPs such as SiO_2, ZrO_2 and TiO_2 by micro-bubble assisted printing did

not form continuous layers due to poor adhesion between the NPs. Addition of binders (such as polyvinylidene difluoride) allowed continuous layered formation, however the deposits were still too porous to act as effective insulating layers. While inorganic metal ion precursors could form oxide layers, these proved to be highly porous or have cracks, rendering them inappropriate for electrical insulation (**Figure S3**). Silicon oxide layers formed from TEOS did not show cracking, and pores were not visible in HR-SEM. This might be attributed to the organic nature of the silicon oxide precursor (TEOS) in contrast with the inorganic precursors of the other oxides used. Although nano-pores were reported for such layers,[51] we hypothesize that they are small enough to prevent penetration of the top metallic layer. However, further investigation beyond the scope of this paper is required to validate this hypothesis.

This laser based microprinting method also enables control over the width and height of fabricated conducting and insulating layers. For silicon oxide (**Figure 5a**), as the power varied from 14 mW to 35 mW, the obtained deposition width increased from about 21 to 50 µm. In addition, the height of the deposits increased with laser power from about 70 to 150 nm. Similar results where found for Pt layers (**Figure 5c,d**). Finally, repeating the deposition procedure several times (silicon oxide deposition on a printed Pt line) by moving the laser back and forth also increased layer height (**Figure 5b**).

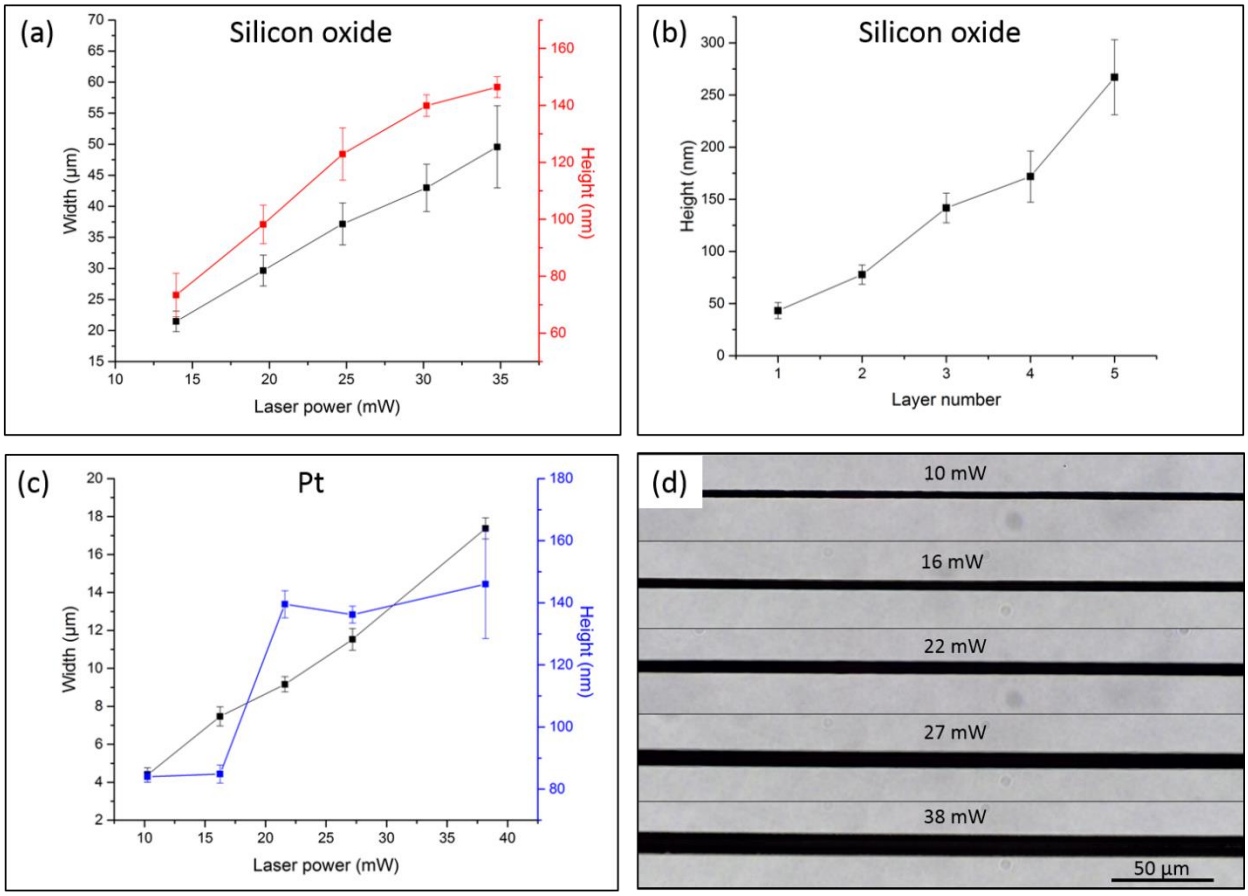

Figure 5. (a) Width and height of silicon oxide lines as a function of laser power and (b) layer number. (c) Width and height of Pt lines as a function of laser power and (d) corresponding bright field microscopy images.

The micro-bubbles that are seen during the deposition process (**Video SV1**) are crucial for material deposition and we've not attained material deposition that was not accompanied by micro-bubble formation. Additionally, when the shutter was set to allow laser illumination of 50 ms, ring shaped patterns were formed (**Figure 6a-d**), indicating material deposition of Pt and silicon oxide at the contact area of the micro-bubble with the underlying surface. Based on previous studies,[36] we suggest that the mechanism combines deposition by thermally driven reactions with micro-

bubble assisted printing (**Figure 6e**). NPs of Pt or silicon oxide are first created, and heat generated by laser light absorption increases the vapor pressure of the liquid until a micro-bubble is formed. When microprinting Pt, the platinum NPs absorb the 532 nm photons, while for silicon oxide, which is transparent, the substrate (previously deposited Pt) absorbs the photon energy. Convection flows at the vicinity of the micro-bubble carry NPs, and some of them are transferred to the microbubble/substrate interface where they are pinned (**Figure 6e**). Thermal reactions also occur at the micro-bubble/substrate interface and form products that fill the gaps between deposited NPs (gray area in **Figure 6e**).[36] Moving the microscope stage relative to the fixed focused laser results in propagation of the microbubble to a new location.[52,53] Therefore, while the deposits are ring-shaped around the base of the micro-bubble, continuously moving the stage provides dense depositions of Pt and silicon oxide. We note that laser modulation was used to allow formation of continuous depositions. Previous studies have shown that modulation allows better control over the size of the microbubble and prevents it from being pinned to the deposited material while moving.[21,36] The increase in both width and height with laser power shown in (**Figure 5a,c,d**) can be rationalized as follows. The increase in absorbed light creates a bigger microbubble, leading to wider lines. The greater amount of absorbed energy also promotes excess material synthesis and deposition, which pile higher.

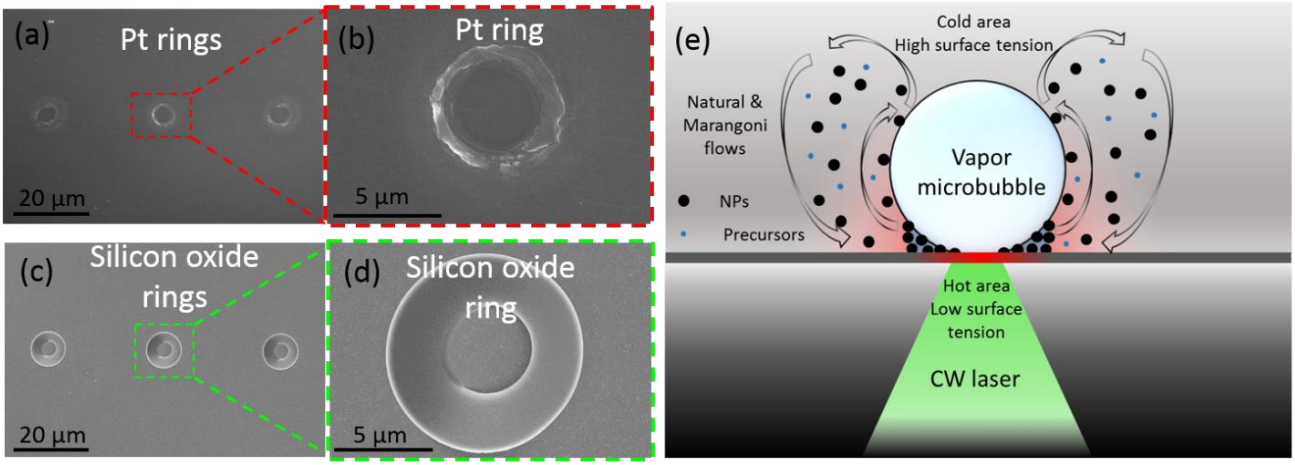

Figure 6. SEM images of (a,b) Pt and (c,d) silicon oxide demonstrating ring-shaped patterns indicative of material deposition at the contact area of a micro-bubble with the underlying surface. (e) Illustration of deposition mechanism by thermally driven reactions with micro-bubble assisted printing. NPs are first created, followed by a microbubble from the vapors of the liquid medium. Convection flows at the vicinity of the micro-bubble carry NPs, and some of them are transferred to the micro-bubble/substrate interface where they are pinned. Thermal reactions also occur at the micro-bubble/substrate interface and form products that fill the gaps between the deposited NPs (gray area).

Junctions with higher complexity levels could also be attained using our approach. **Figure 7a** demonstrates a five-layered junction consisting of three Pt lines separated by two silicon oxide layers as illustrated in **Figure 7b**. I-V measurements (**Figure 7c**) indicate conductance of the Pt lines while the high resistivity of silicon oxide layers is maintained. Two interwoven junctions with a ~5-micron separation are shown and illustrated in **Figure 7d-f**. Corresponding I-V curves are presented in **Figure 7g**. Deposition of narrower silicon oxide layers (compared to what has been shown above) was achieved using laser power of 8.5mW and stage velocity of 600 µm/s. We note that line spacing of conducting lines can be further reduced (**Figure S4**). Additionally,

junctions could be formed by a combination of more than one metal as the conducting element. This was demonstrated by forming a junction of Au/silicon-oxide/Pt (**Figure S5**).

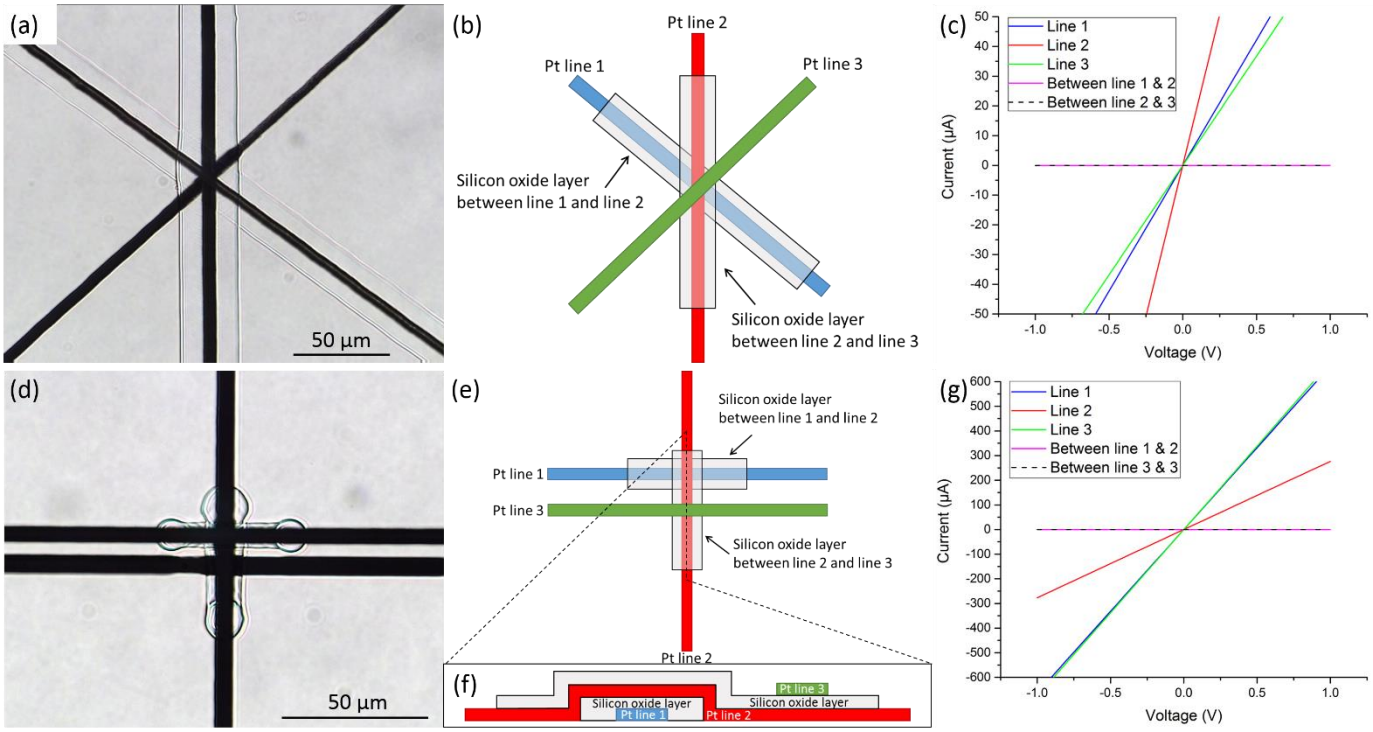

Figure 7. (a) Bright-field microscopy image, (b) illustration and (c) corresponding I-V measurements of a five-layered junction. (d) Bright-field microscopy image, (e-f) illustrations (not to scale) and (g) corresponding I-V measurements of two interwoven junctions with a ~5-micron separation.

Finally, we introduce a new concept where microfluidics is utilized to enhance the capabilities of multi-layered laser microprinting. The study presented above requires manually removing the liquid precursors of one component before applying the second component. This is a time consuming and error-prone process, which makes this approach unpractical if many layers are required. We therefore suggest using pressure controlled microfluidic channels to quickly switch

between precursors (**Figure 8a**), allowing faster production of conducting/insulating/conducting multi-layered micro-structures. A polydimethylsiloxane (PDMS) micro-channel (2 mm wide × 100 μm high) was formed by standard lithographic methods and was attached to a glass slide on which our microprinting took place. The micro-channel was connected at both edges by polytetrafluoroethylene (PTFE) tubes. The Pt based precursor was inserted into one of the tubes, while the TEOS based precursor was inserted into the other. Air deliberately trapped in-between the two precursors, functioned as a separator. Both tubes were connected to a microfluidic pressure-based flow controller. This configuration (**Figure 8b**) allowed us to select which precursor would be placed inside the microfluidic channel where laser microprinting is performed. We repeatedly switched between precursors (**Figure 8a** and **Video SV2**) to form multi-layered structures visualized in a HR-SEM image (**Figure 8c**). **Figure 8d**,**e** show EDS mappings of Pt and Si, respectively. Switching between precursors in this setup took approximately ten seconds, a major improvement over previous manual methods. However, we did not optimize this process. Reducing the amount of air and increasing the flow velocity could lead to substantially lower transition times. Micro-printing multiple elements on larger areas could conceptually be achieved utilizing microfluidics by increasing the micro-channel width, using several micro-channels, or shifting the micro-channel from region to region.

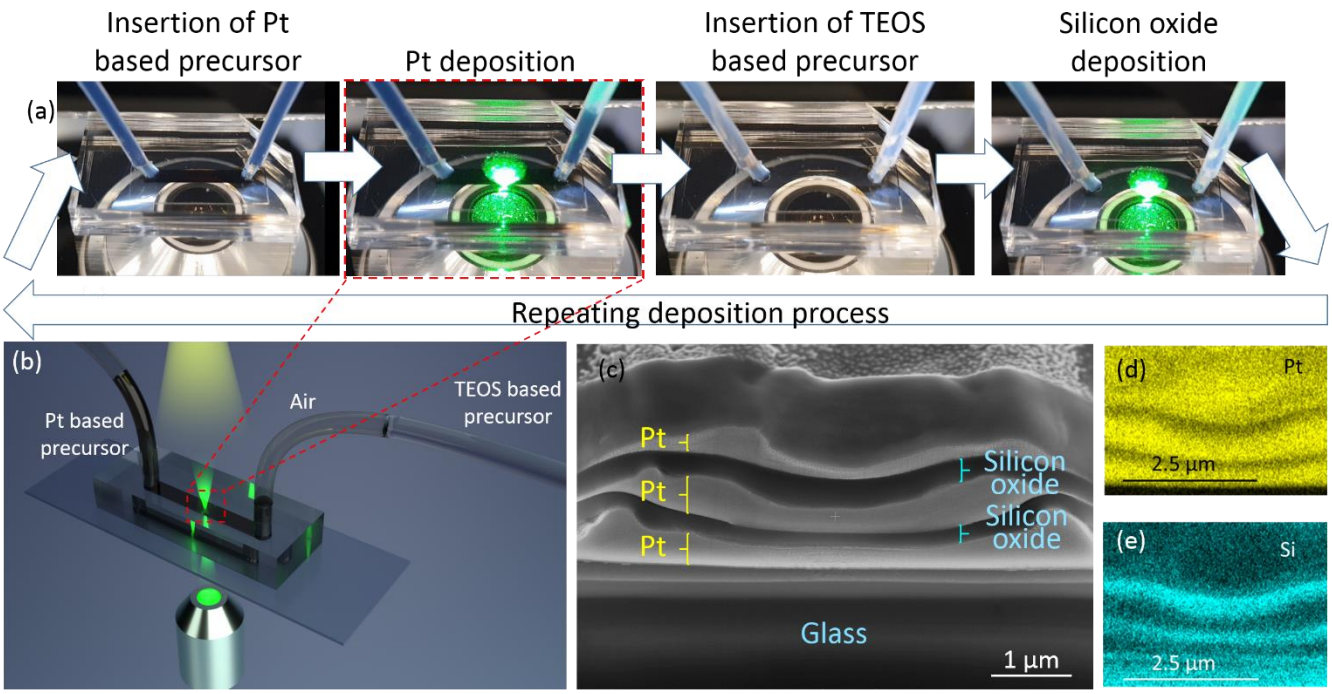

Figure 8. Microfluidic configuration utilized for multi-layered laser micro-printing, allowing faster and more reliable production of conducting/insulating/conducting micro-structures. (a) Images of the printing process displaying the steps for printing Pt and silicon oxide layers. This process can be repeated several times. (b) Illustration of the combined laser printing and microfluidic setup. A microfluidic channel is connected at both edges by tubes. Air is used as a separator between the two precursors inserted into the tubes. A pressure-based microfluidic flow controller is used to select which precursor is placed on the glass substrate and deposited by laser microprinting. (c) HR-SEM image and (d,e) EDS mapping of FIB cross-sectioned multi-layered micro-structure fabricated using the microfluidic channel.

CONCLUSIONS

In conclusion, laser based microprinting of layered conducting/insulating/conducting micro-structures was demonstrated with silicon oxide in between platinum conducting layers. Several configurations were shown, and cross-sections of the micro-structures were visualized by HR-

SEM and mapped with EDS. Electrical transport measurements were performed to examine the properties of the insulating layer, yielding sufficiently high resistivity of 1.5×10^{11} Ωm at 0.5 V. Control over the width and height of the insulating layer was demonstrated by increasing the laser power and number of iterations. Finally, microfluidics were utilized to eliminate the manual, time consuming, and error-prone process of switching between precursors. This novel approach could prove beneficial for fabrication of various multi-layered micro-electronic devices.

EXPERIMENTAL

Sample preparation

Pt was chosen due to its good adhesion to the substrate. For the preparation of 3 wt% Pt based precursor, 30 mg of $Pt(II)Cl_2$ and 0.97 g of dry NMP (Acros Organics) were added to a glass vial and stirred on a tube roller at room temperature for a week. The obtained Pt based precursor was filtered using a syringe filter (poly-tetrafluoroethylene, Memebrane Solutions) with 0.4 μm pore size before microprinting. Note that NMP was chosen due to its relatively high boiling point (202 °C), which is preferrable for both microbubble assisted printing and thermal synthesis.[23] NMP also promotes the thermal reduction process of Pt ions to a stable dispersion of Pt NPs. The detailed chemical mechanism of metal ion reduction by NMP is not yet fully understood.[54]

The TEOS precursor solution was prepared by adding 725 μL of NMP to 250 μL of TEOS (Aldrich) followed by mixing with a vortex shaker. Then, 25 μL of 2M NaOH (Fisher Scientific) in deionized water were slowly added while stirring. The obtained precursor was passed through a 0.4 μm pore size syringe filter before microprinting.

Sample preparation consisted of cleaning microscope cover glass slides (0.17 mm thick) with isopropanol, followed by drying. A cavity was formed by placing one of the cover slides as a spacer in-between two slides. Using a pipette, 50 μL of the Pt or TEOS based precursors were

inserted by capillary force into the cavity. A glass substrate sputtered with 5 nm of Cr followed by 100 nm of gold was used for conductivity and resistivity measurements as well as results shown in **Figure 5a** and **Figure 6a-d**.

Optical setup

The optical setup (**Figure 1a**) consists of a CW laser beam (532 nm, Verdi G-Serie, Coherent) integrated with a bright-field inverted microscope (Nikon Eclipse Ti-U) and focused by a 40× objective lens (0.6 NA, Nikon). The laser power, as measured after the objective lens with a power meter (PM100, Thorlabs) and without applying the modulation, was 14 mW unless otherwise stated. The stage of the microscope was computer-controlled, and the experiments were recorded using a CMOS camera (DPCAM 6CHDMI, DeltaPix). To produce the micro-structures, the microscope stage was moved with a stage velocity of 100 µm/s for Pt and 400 µm/s for silicon oxide unless stated otherwise. Laser modulation for Pt patterns was performed by an optical chopper (Thorlabs) with a frequency of 3 kHz and duty cycle of 50%. The ring-shaped patterns of both Pt and silicon oxide (**Figure 6a-d**) were formed by limiting the exposure time of the laser beam to 50 ms by a mechanical shutter (SH1, Thorlabs).

Microfluidic channel fabrication and setup

A mixture of dimethylsiloxane and crosslinking agents (Sylgard 184) was poured on a mold containing the positive relief of the channel's layout prepared using conventional photolithography. Curing was obtained at 80 °C for two hours. After curing, the PDMS layer was detached from the mold, forming an open micro-channel. Holes were punched in the PDMS to allow tube connection. A clean glass slide (1 mm thick) was attached to the micro-channel followed by 12 hours at 80 °C. Usually, plasma treatment is preferred for the PDMS micro-channel

and glass to strengthen the bond between them and permanently attach them together. However, as access to the glass substrate is required after micro-patterning and imaging, plasma treatment was avoided. The final microfluidic device contains a single channel, 2 mm wide, 100 µm high, and 10–30 mm long. The micro-channel was connected at both edges by PTFE tubes. The Pt and TEOS based precursors were inserted into the tubes with air functioning as a separator deliberately trapped in-between. Both tubes were connected to a microfluidic pressure-based flow controller (Elveflow OB1 MK3 system).

Characterization methods

HR-SEM imaging, FIB cross-sectioning and EDS measurements were performed using a Helios 5 UC, dual-beam system (Thermo Fisher Scientific). The nanostructure was considered with transmission electron microscopy on a JEOL-2010 HR-TEM, using an accelerating voltage of 200 kV, and elemental analysis was conducted by Energy Dispersive X-ray Spectroscopy (EDS) with a spot size of 35nm. SADP measurements were performed with an accelerating voltage of 200 kV and a spot size of 400nm.

Raman measurements were performed using a customized setup based on a Zeiss Axio Vario Scope A1 microscope equipped with a 785 nm laser with a power of 50 mW. 600 l/mm grating and a 50× objective lens were used. Resistance measurements were performed at a SUSS MicroTec probe station. Local electrical conductivity was measured using a MultiMode AFM system (Bruker AXS) equipped with a high sensitive current detector (TUNA module) with a set point of 0.47 V. All images were obtained using TUNA mode with a SCM-PIC-V2 (Bruker) Pt/Ir coated silicon probe (spring constant of 0.2 N/m). The resonance frequency of the cantilever was approximately 13 kHz (in air). The measurements were performed under environmental conditions. The images

were captured in the retrace direction with a scan rate of 0.5 Hz. The resolution of the images was 512 samples/line. Image processing was performed using Nanoscope Analysis software. Prior to analysis, the "flatting" and "planefit" functions were applied to each image.

Widths, heights, and cross-sectional areas of deposited Pt layers were obtained by an optical profilometer (LEXT, OLS4100, Olympus), while for silicon oxide layers a stylus profilometer (Veeco Dektak 150 system) was used. Measurements for **Figure 5a-c** were performed on three samples prepared separately, each containing at least ten lines. Reported heights were calculated by dividing the cross-sectional area with the width (providing an average height). Only for silicon oxide deposited on a Pt line (and not on a flat surface), the height was determined as the difference between maximum heights. Conductance of deposited Pt lines (15 separate samples) were measured by a Keithley 2400 source-meter equipped with a home built 4-probe station.

ASSOCIATED CONTENT

Supporting Information.

SEM images of attempts to form insulating layers from Al based ionic solution (PDF); Movie showing micro-printing of a multi-layered junction (MP4); Movie showing fabrication of a multi-layered micro-structure inside a microfluidic channel (MP4);

AUTHOR INFORMATION

Corresponding Author

*E-mail: hagay.shpaisman@biu.ac.il

Funding Sources

This research was partially supported by the Israeli Science Foundation (grant No. 952/19).

Notes

The authors declare no competing financial interest.

ACKNOWLEDGMENT

The authors acknowledge Talia Sharabani for technical assistance with sputtering, Dr. Omer Yaffe for his help with Raman measurements and analysis, and Dr. Yuval Elias for scientific editing.

REFERENCES

(1) Salim, A.; Lim, S. Review of Recent Inkjet-Printed Capacitive Tactile Sensors. *Sensors* **2017**, *17* (11), 2593. https://doi.org/10.3390/s17112593.

(2) Kang, B. J.; Lee, C. K.; Oh, J. H. All-Inkjet-Printed Electrical Components and Circuit Fabrication on a Plastic Substrate. *Microelectronic Engineering* **2012**, *97*, 251–254. https://doi.org/10.1016/j.mee.2012.03.032.

(3) Kleemann, H.; Krechan, K.; Fischer, A.; Leo, K. A Review of Vertical Organic Transistors. *Adv. Funct. Mater.* **2020**, *30* (20), 1907113. https://doi.org/10.1002/adfm.201907113.

(4) Saengchairat, N.; Tran, T.; Chua, C.-K. A Review: Additive Manufacturing for Active Electronic Components. *Virtual and Physical Prototyping* **2017**, *12* (1), 31–46. https://doi.org/10.1080/17452759.2016.1253181.

(5) Canal Marques, A.; Cabrera, J.-M.; de Fraga Malfatti, C. Printed Circuit Boards: A Review on the Perspective of Sustainability. *Journal of Environmental Management* **2013**, *131*, 298–306. https://doi.org/10.1016/j.jenvman.2013.10.003.

(6) Tsai, H.-W.; Pei, Z.; Chan, Y.-J. A Conductor/Insulator/Conductor Complex Layer at Anode for Current Enhancement in a Polymer Solar Cell. *Appl. Phys. Lett.* **2008**, *93* (7), 073310. https://doi.org/10.1063/1.2974087.

(7) Yu, K. J.; Kuzum, D.; Hwang, S.-W.; Kim, B. H.; Juul, H.; Kim, N. H.; Won, S. M.; Chiang, K.; Trumpis, M.; Richardson, A. G.; Cheng, H.; Fang, H.; Thompson, M.; Bink, H.; Talos, D.; Seo, K. J.; Lee, H. N.; Kang, S.-K.; Kim, J.-H.; Lee, J. Y.; Huang, Y.; Jensen, F. E.; Dichter, M. A.; Lucas, T. H.; Viventi, J.; Litt, B.; Rogers, J. A. Bioresorbable Silicon Electronics for Transient Spatiotemporal Mapping of Electrical Activity from the Cerebral Cortex. *Nature Mater* **2016**, *15* (7), 782–791. https://doi.org/10.1038/nmat4624.

(8) Zhang, Z.; Ye, Y.; Pu, C.; Deng, Y.; Dai, X.; Chen, X.; Chen, D.; Zheng, X.; Gao, Y.; Fang, W.; Peng, X.; Jin, Y. High-Performance, Solution-Processed, and Insulating-Layer-Free

Light-Emitting Diodes Based on Colloidal Quantum Dots. *Adv. Mater.* **2018**, *30* (28), 1801387. https://doi.org/10.1002/adma.201801387.
(9) Kumar, B.; Kaushik, B. K.; Negi, Y. S. Organic Thin Film Transistors: Structures, Models, Materials, Fabrication, and Applications: A Review. *Polymer Reviews* **2014**, *54* (1), 33–111. https://doi.org/10.1080/15583724.2013.848455.
(10) Wallace, R. M. Dielectric Materials for Microelectronics. In *Springer Handbook of Electronic and Photonic Materials*; Kasap, S., Capper, P., Eds.; Springer International Publishing: Cham, 2017; pp 1–1. https://doi.org/10.1007/978-3-319-48933-9_27.
(11) Reese, C.; Roberts, M.; Ling, M.; Bao, Z. Organic Thin Film Transistors. *Materials Today* **2004**, *7* (9), 20–27. https://doi.org/10.1016/S1369-7021(04)00398-0.
(12) Chen, Y. Nanofabrication by Electron Beam Lithography and Its Applications: A Review. *Microelectronic Engineering* **2015**, *135*, 57–72. https://doi.org/10.1016/j.mee.2015.02.042.
(13) Wu, B.; Kumar, A. Extreme Ultraviolet Lithography: A Review. *J. Vac. Sci. Technol. B* **2007**, *25* (6), 1743. https://doi.org/10.1116/1.2794048.
(14) Mattana, G.; Loi, A.; Woytasik, M.; Barbaro, M.; Noël, V.; Piro, B. Inkjet-Printing: A New Fabrication Technology for Organic Transistors. *Adv. Mater. Technol.* **2017**, *2* (10), 1700063. https://doi.org/10.1002/admt.201700063.
(15) Lu, S.; Cardenas, J. A.; Worsley, R.; Williams, N. X.; Andrews, J. B.; Casiraghi, C.; Franklin, A. D. Flexible, Print-in-Place 1D–2D Thin-Film Transistors Using Aerosol Jet Printing. *ACS Nano* **2019**, *13* (10), 11263–11272. https://doi.org/10.1021/acsnano.9b04337.
(16) Wilkinson, N. J.; Smith, M. A. A.; Kay, R. W.; Harris, R. A. A Review of Aerosol Jet Printing—a Non-Traditional Hybrid Process for Micro-Manufacturing. *Int J Adv Manuf Technol* **2019**, *105* (11), 4599–4619. https://doi.org/10.1007/s00170-019-03438-2.
(17) Choi, J.-W.; Kim, H.-C.; Wicker, R. Multi-Material Stereolithography. *Journal of Materials Processing Technology* **2011**, *211* (3), 318–328. https://doi.org/10.1016/j.jmatprotec.2010.10.003.
(18) Lopes, A. J.; Lee, I. H.; MacDonald, E.; Quintana, R.; Wicker, R. Laser Curing of Silver-Based Conductive Inks for in Situ 3D Structural Electronics Fabrication in Stereolithography. *Journal of Materials Processing Technology* **2014**, *214* (9), 1935–1945. https://doi.org/10.1016/j.jmatprotec.2014.04.009.
(19) Li, W.-D.; Wang, C.; Jiang, Z.-H.; Chen, L.-J.; Wei, Y.-H.; Zhang, L.-Y.; Chen, M.-Y.; Yang, X.; Zhang, G.-J. Stereolithography Based Additive Manufacturing of High-k Polymer Matrix Composites Facilitated by Thermal Plasma Processed Barium Titanate Microspheres. *Materials & Design* **2020**, *192*, 108733. https://doi.org/10.1016/j.matdes.2020.108733.
(20) Armon, N.; Greenberg, E.; Edri, E.; Ornit Nagler-Avramovitz; Elias, Y.; Shpaisman, H. Laser Based Printing: From Liquids to Microstructures. *Adv. Funct. Mater. 2008547*. https://doi.org/10.1002/adfm.202008547.
(21) Armon, N.; Greenberg, E.; Layani, M.; Rosen, Y. S.; Magdassi, S.; Shpaisman, H. Continuous Nanoparticle Assembly by a Modulated Photo-Induced Microbubble for Fabrication of Micrometric Conductive Patterns. *ACS Applied Materials & Interfaces* **2017**, *9* (50), 44214–44221. https://doi.org/10.1021/acsami.7b14614.
(22) Rahamim, G.; Greenberg, E.; Rajouâ, K.; Favier, F.; Shpaisman, H.; Zitoun, D. Laser-Induced Colloidal Writing of Organometallic Precursor–Based Repeatable and Fast Pd–Ni Hydrogen Sensor. *Adv. Mater. Interfaces* **2019**, *6* (19), 1900768. https://doi.org/10.1002/admi.201900768.

(23) Edri, E.; Armon, N.; Greenberg, E.; Hadad, E.; Bockstaller, M. R.; Shpaisman, H. Assembly of Conductive Polyaniline Microstructures by a Laser-Induced Microbubble. *ACS Appl. Mater. Interfaces* **2020**, *12* (19), 22278–22286. https://doi.org/10.1021/acsami.0c00904.

(24) Lin, L.; Peng, X.; Mao, Z.; Li, W.; Yogeesh, M. N.; Rajeeva, B. B.; Perillo, E. P.; Dunn, A. K.; Akinwande, D.; Zheng, Y. Bubble-Pen Lithography. *Nano Letters* **2016**, *16* (1), 701–708. https://doi.org/10.1021/acs.nanolett.5b04524.

(25) Zheng, Y.; Liu, H.; Wang, Y.; Zhu, C.; Wang, S.; Cao, J.; Zhu, S. Accumulating Microparticles and Direct-Writing Micropatterns Using a Continuous-Wave Laser-Induced Vapor Bubble. *Lab on a Chip* **2011**, *11* (22), 3816–3820. https://doi.org/10.1039/c1lc20478e.

(26) Roy, B.; Arya, M.; Thomas, P.; Jürgschat, J. K.; Venkata Rao, K.; Banerjee, A.; Malla Reddy, C.; Roy, S. Self-Assembly of Mesoscopic Materials To Form Controlled and Continuous Patterns by Thermo-Optically Manipulated Laser Induced Microbubbles. *Langmuir* **2013**, *29* (47), 14733–14742. https://doi.org/10.1021/la402777e.

(27) Zarzar, L. D.; Swartzentruber, B. S.; Donovan, B. F.; Hopkins, P. E.; Kaehr, B. Using Laser-Induced Thermal Voxels to Pattern Diverse Materials at the Solid–Liquid Interface. *ACS Applied Materials & Interfaces* **2016**, *8* (33), 21134–21139. https://doi.org/10.1021/acsami.6b06625.

(28) Lachish-Zalait, A.; Zbaida, D.; Klein, E.; Elbaum, M. Direct Surface Patterning from Solutions: Localized Microchemistry Using a Focused Laser. *Advanced Functional Materials* **2001**, *11* (3), 218–223. https://doi.org/10.1002/1616-3028(200106)11:3<218::AID-ADFM218>3.0.CO;2-T.

(29) Zhou, X.; Guo, W.; Zhu, Y.; Peng, P. The Laser Writing of Highly Conductive and Anti-Oxidative Copper Structures in Liquid. *Nanoscale* **2019**, 10.1039.C9NR07248A. https://doi.org/10.1039/C9NR07248A.

(30) Kindle, C.; Castonguay, A.; McGee, S.; Tomko, J. A.; Hopkins, P. E.; Zarzar, L. D. Direct Laser Writing from Aqueous Precursors for Nano to Microscale Topographical Control, Integration, and Synthesis of Nanocrystalline Mixed Metal Oxides. *ACS Appl. Nano Mater.* **2019**, *2* (5), 2581–2586. https://doi.org/10.1021/acsanm.9b00360.

(31) Yeo, J.; Hong, S.; Kim, G.; Lee, H.; Suh, Y. D.; Park, I.; Grigoropoulos, C. P.; Ko, S. H. Laser-Induced Hydrothermal Growth of Heterogeneous Metal-Oxide Nanowire on Flexible Substrate by Laser Absorption Layer Design. *ACS Nano* **2015**, *9* (6), 6059–6068. https://doi.org/10.1021/acsnano.5b01125.

(32) Yeo, J.; Hong, S.; Manorotkul, W.; Suh, Y. D.; Lee, J.; Kwon, J.; Ko, S. H. Digital 3D Local Growth of Iron Oxide Micro- and Nanorods by Laser-Induced Photothermal Chemical Liquid Growth. *The Journal of Physical Chemistry C* **2014**, *118* (28), 15448–15454. https://doi.org/10.1021/jp501642j.

(33) Yeo, J.; Hong, S.; Wanit, M.; Kang, H. W.; Lee, D.; Grigoropoulos, C. P.; Sung, H. J.; Ko, S. H. Rapid, One-Step, Digital Selective Growth of ZnO Nanowires on 3D Structures Using Laser Induced Hydrothermal Growth. *Adv. Funct. Mater.* **2013**, *23* (26), 3316–3323. https://doi.org/10.1002/adfm.201203863.

(34) Xie, Y.; Yang, S.; Mao, Z.; Li, P.; Zhao, C.; Cohick, Z.; Huang, P.-H.; Huang, T. J. *In Situ* Fabrication of 3D Ag@ZnO Nanostructures for Microfluidic Surface-Enhanced Raman Scattering Systems. *ACS Nano* **2014**, *8* (12), 12175–12184. https://doi.org/10.1021/nn503826r.

(35) Zbaida, D.; Popovitz-Biro, R.; Lachish-Zalait, A.; Klein, E.; Wachtel, E.; Prior, Y.; Elbaum, M. Laser-Induced Direct Lithography for Patterning of Carbon with Sp3 and Sp2 Hybridization. *Advanced Functional Materials* **2003**, *13* (5), 412–417. https://doi.org/10.1002/adfm.200304318.

(36) Greenberg, E.; Armon, N.; Kapon, O.; Ben-Ishai, M.; Shpaisman, H. Nanostructure and Mechanism of Metal Deposition by a Laser-Induced Photothermal Reaction. *Advanced Materials Interfaces* **2019**, *6* (14), 1900541. https://doi.org/10.1002/admi.201900541.

(37) Fujii, S.; Fukano, R.; Hayami, Y.; Ozawa, H.; Muneyuki, E.; Kitamura, N.; Haga, M. Simultaneous Formation and Spatial Patterning of ZnO on ITO Surfaces by Local Laser-Induced Generation of Microbubbles in Aqueous Solutions of $[Zn(NH_3)_4]^{2+}$. *ACS Applied Materials & Interfaces* **2017**, *9* (9), 8413–8419. https://doi.org/10.1021/acsami.6b16719.

(38) Ghosh, S.; Das, S.; Paul, S.; Thomas, P.; Roy, B.; Mitra, P.; Roy, S.; Banerjee, A. In Situ Self-Assembly and Photopolymerization for Hetero-Phase Synthesis and Patterning of Conducting Materials Using Soft Oxometalates in Thermo-Optical Tweezers. *J. Mater. Chem. C* **2017**, *5* (27), 6718–6728. https://doi.org/10.1039/C7TC01941F.

(39) Armon, N.; Greenberg, E.; Edri, E.; Kenigsberg, A.; Piperno, S.; Kapon, O.; Fleker, O.; Perelshtein, I.; Cohen-Taguri, G.; Hod, I.; Shpaisman, H. Simultaneous Laser-Induced Synthesis and Micro-Patterning of a Metal Organic Framework. *Chem. Commun.* **2019**, 10.1039.C9CC05990C. https://doi.org/10.1039/C9CC05990C.

(40) Rajeeva, B. B.; Kunal, P.; Kollipara, P. S.; Acharya, P. V.; Joe, M.; Ide, M. S.; Jarvis, K.; Liu, Y.; Bahadur, V.; Humphrey, S. M.; Zheng, Y. Accumulation-Driven Unified Spatiotemporal Synthesis and Structuring of Immiscible Metallic Nanoalloys. *Matter* **2019**, S2590238519302875. https://doi.org/10.1016/j.matt.2019.10.017.

(41) Scott, J. F.; Porto, S. P. S. Longitudinal and Transverse Optical Lattice Vibrations in Quartz. *Phys. Rev.* **1967**, *161* (3), 903–910. https://doi.org/10.1103/PhysRev.161.903.

(42) Biswas, R. K.; Khan, P.; Mukherjee, S.; Mukhopadhyay, A. K.; Ghosh, J.; Muraleedharan, K. Study of Short Range Structure of Amorphous Silica from PDF Using Ag Radiation in Laboratory XRD System, RAMAN and NEXAFS. *Journal of Non-Crystalline Solids* **2018**, *488*, 1–9. https://doi.org/10.1016/j.jnoncrysol.2018.02.037.

(43) Humbert, B.; Burneau, A.; Gallas, J. P.; Lavalley, J. C. Origin of the Raman Bands, D1 and D2, in High Surface Area and Vitreous Silicas. *Journal of Non-Crystalline Solids* **1992**, *143*, 75–83. https://doi.org/10.1016/S0022-3093(05)80555-1.

(44) Brinker, C. J.; Tallant, D. R.; Roth, E. P.; Ashley, C. S. Sol-Gel Transition in Simple Silicates. *Journal of Non-Crystalline Solids* **1986**, *82* (1–3), 117–126. https://doi.org/10.1016/0022-3093(86)90119-5.

(45) Matsui, K.; Satoh, H.; Kyoto, M. Raman Spectra of Silica Gel Prepared from Triethoxysilane and Tetraethoxysilane by the Sol-Gel Method. *Nippon Seramikkusu Kyokai gakujutsu ronbunshi* **1998**, *106* (1233), 528–530. https://doi.org/10.2109/jcersj.106.528.

(46) de Ferri, L.; Lorenzi, A.; Lottici, P. P. OctTES/TEOS System for Hybrid Coatings: Real-Time Monitoring of the Hydrolysis and Condensation by Raman Spectroscopy: OctTES/TEOS System for Hybrid Coatings. *J. Raman Spectrosc.* **2016**, *47* (6), 699–705. https://doi.org/10.1002/jrs.4881.

(47) Walrafen, G. E.; Hokmabadi, M. S.; Holmes, N. C. Raman Spectrum and Structure of Thermally Treated Silica Aerogel. *The Journal of Chemical Physics* **1986**, *85* (2), 771–776. https://doi.org/10.1063/1.451284.

(48) Mulder, C. A. M. Defect Structures in Silica Glass. *Journal of Non-Crystalline Solids* **1987**, *95–96*, 303–310. https://doi.org/10.1016/S0022-3093(87)80124-2.
(49) Zarzar, L. D.; Swartzentruber, B. S.; Harper, J. C.; Dunphy, D. R.; Brinker, C. J.; Aizenberg, J.; Kaehr, B. Multiphoton Lithography of Nanocrystalline Platinum and Palladium for Site-Specific Catalysis in 3D Microenvironments. *J. Am. Chem. Soc.* **2012**, *134* (9), 4007–4010. https://doi.org/10.1021/ja211602t.
(50) Anderson, J. H.; Parks, G. A. Electrical Conductivity of Silica Gel in the Presence of Adsorbed Water. *J. Phys. Chem.* **1968**, *72* (10), 3662–3668. https://doi.org/10.1021/j100856a051.
(51) Kajihara, K. Recent Advances in Sol–Gel Synthesis of Monolithic Silica and Silica-Based Glasses. *Journal of Asian Ceramic Societies* **2013**, *1* (2), 121–133. https://doi.org/10.1016/j.jascer.2013.04.002.
(52) Zhang, Q.; Pang, Y.; Schiffbauer, J.; Jemcov, A.; Chang, H.-C.; Lee, E.; Luo, T. Light-Guided Surface Plasmonic Bubble Movement via Contact Line De-Pinning by In-Situ Deposited Plasmonic Nanoparticle Heating. *ACS Applied Materials & Interfaces* **2019**, *11* (51), 48525–48532. https://doi.org/10.1021/acsami.9b16067.
(53) Zhang, Q.; Neal, R. D.; Huang, D.; Neretina, S.; Lee, E.; Luo, T. Surface Bubble Growth in Plasmonic Nanoparticle Suspension. *ACS Appl. Mater. Interfaces* **2020**, *12* (23), 26680–26687. https://doi.org/10.1021/acsami.0c05448.
(54) Kakade, B. A.; Tamaki, T.; Ohashi, H.; Yamaguchi, T. Highly Active Bimetallic PdPt and CoPt Nanocrystals for Methanol Electro-Oxidation. *J. Phys. Chem. C* **2012**, *116* (13), 7464–7470. https://doi.org/10.1021/jp300140s.

For Table of Contents Only

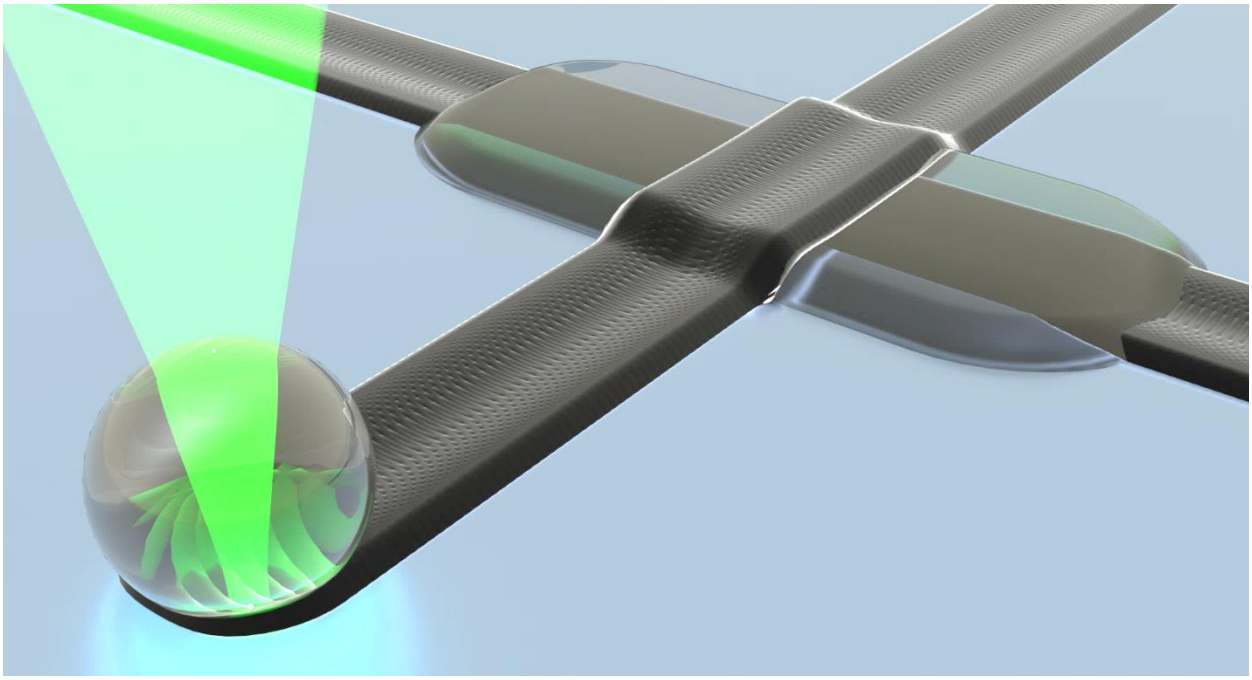

Supporting Information

Laser printing of multi-layered alternately conducting and insulating micro-structures

Eitan Edri,[1,2] Nina Armon,[1,2] Ehud Greenberg,[1,2] Shlomit Moshe-Tsurel,[1,2] Danielle Lubotzky,[1,2] Tommaso Salzillo,[3] Ilana Perelshtein,[2] Maria Tkachev,[2] Olga Girshevitz[2] and Hagay Shpaisman[,1,2]*

[1] Department of Chemistry, Bar-Ilan University, Ramat Gan 5290002, Israel

[2] Institute of Nanotechnology and Advanced Materials (BINA), Bar-Ilan University, Ramat Gan 5290002, Israel

[3] Department of Chemical and Biological Physics, Weizmann Institute of Science, Rehovot 76100, Israel

*E-mail: hagay.shpaisman@biu.ac.il

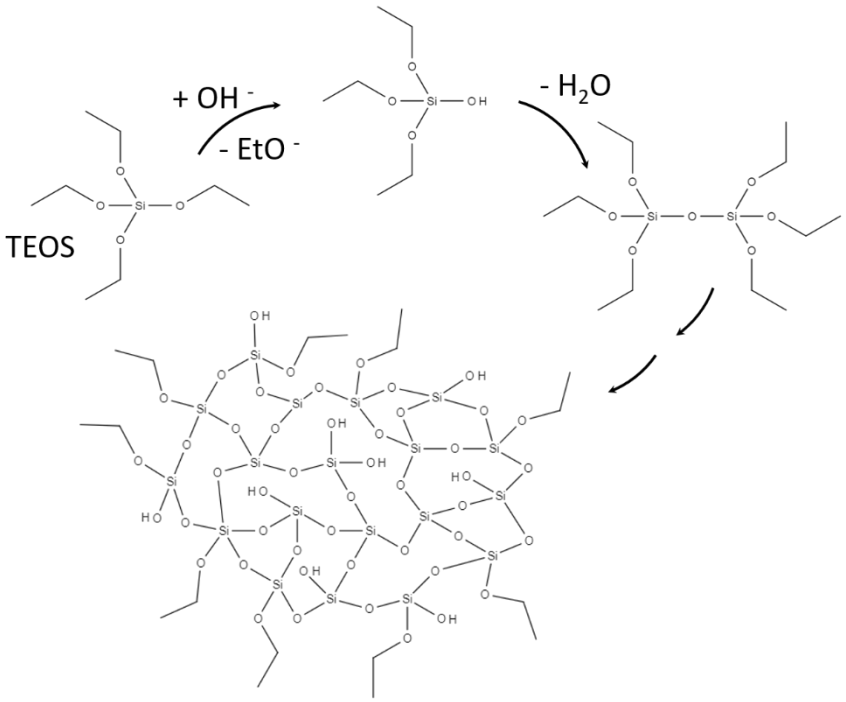

Figure S1. Synthesis scheme showing condensation polymerization of TEOS to form silicon oxide.

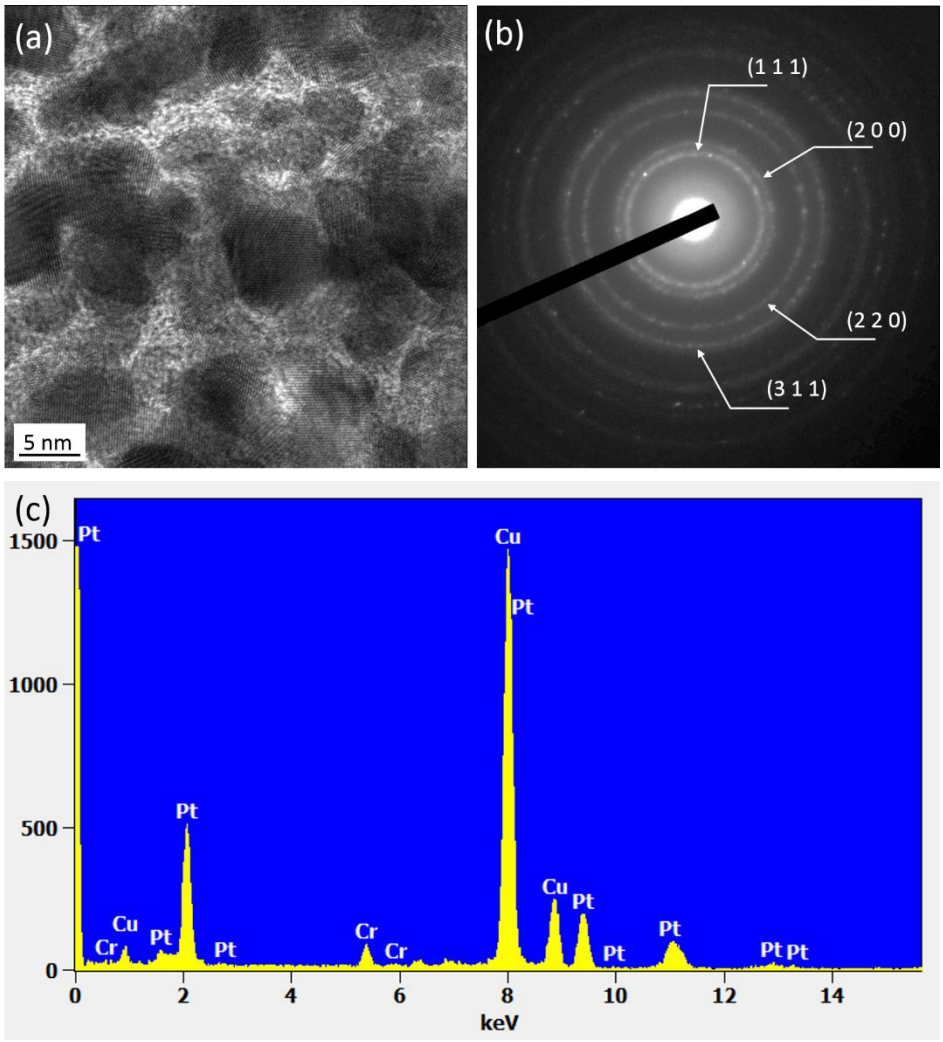

Figure S2. (a) HR-TEM image of prepared lamella from a deposited Pt line. (b) Selected area diffraction pattern measurements showing d-spacing of 2.25 Å, 1.90 Å, 1.35 Å and 1.13 Å which are in good correlation with (1 1 1), (2 0 0), (2 2 0) and (3 1 1) planes of fcc Pt, respectively, as reported by the joint committee on powder diffraction standards (JCPDS) file no: 01-087-0646. (c) EDS measurements of the Pt lamella. We note that the Cu and Cr signals arise from the TEM grid and column.

Micro-printing of other possible insulators:

Prior to our findings on micro-printing of insulating silicon oxide, we examined various materials that were expected to form suitable insulating layers. However, the materials listed below did not show reasonable insulating properties.

Dispersions of NPs:

Dispersions of 0.5–1 wt% of SiO_2 (7 nm), ZrO_2 (50 nm) and TiO_2 (50, 100 nm) were prepared in three solvents – water, diethylene glycol dibutyl ether (DB, Alfa Aesar), and N-methyl-2-pyrrolidone (NMP). In all cases, deposition by micro-bubble assisted printing did not form continuous layers due to poor adhesion between the NPs. Addition of 0.1 wt% of polyvinylidene difluoride to serve as a binder allowed continuous layered formation, however the deposits were too porous to act as effective insulating layers.

Solutions containing inorganic precursors:

Solutions of 3 wt% of $AlCl_3$ (Fluka) were prepared in DB, NMP, and water. Depositions by a combination of thermally driven reactions with micro-bubble assisted printing on top of Pt lines resulted in porous layers (**Figure S2a**). Addition of 0.5 wt% polyvinyl alcohol (PVOH, Aldrich) showed no improvement (**Figure S2b**). Solutions of 3 wt% $Al(NO_3)_3$ (Merck) in a 0.5 M NaOH solution with and without 0.5 wt% PVOH were also prepared; depositions on Pt lines by thermally driven reactions with micro-bubble assisted printing formed layers with cracks visible in SEM (**Figure S2c**,**d**). These layers were found to be non-insulating. Depositions from solutions of 15 wt% of $TiCl_3$ in 10% HCl (Merck) and 3 wt% of $(NH_4)_6Mo_7O_{24}$ (Fisher Scientific) in water also failed to form insulating layers.

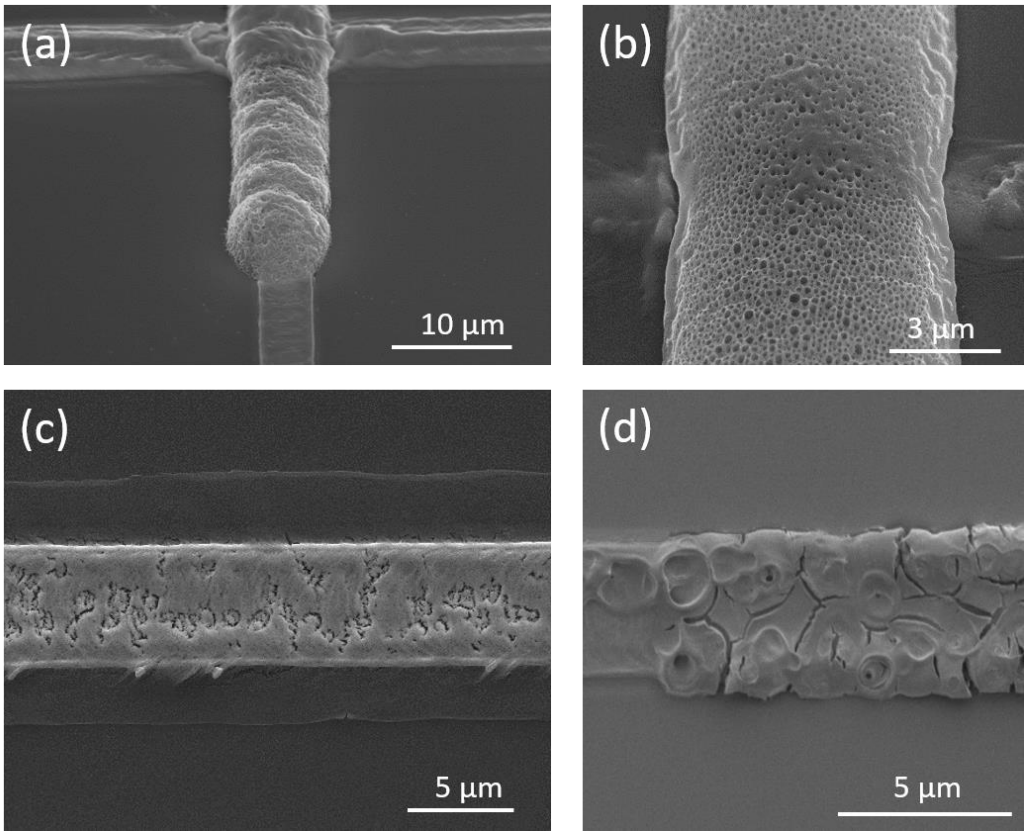

Figure S3. SEM images of depositions fabricated by thermally driven reactions with micro-bubble assisted printing on top of a Pt line that failed to form an insulating layer. The precursors used were: (a) 3 wt% $AlCl_3$ in water, (b) 3 wt% $AlCl_3$ in water with 0.5 wt% polyvinyl alcohol, (c) 3 wt% $Al(NO_3)_3$ in a 0.5M NaOH solution and (d) 3 wt% $Al(NO_3)_3$ with 0.5 wt% PVOH.

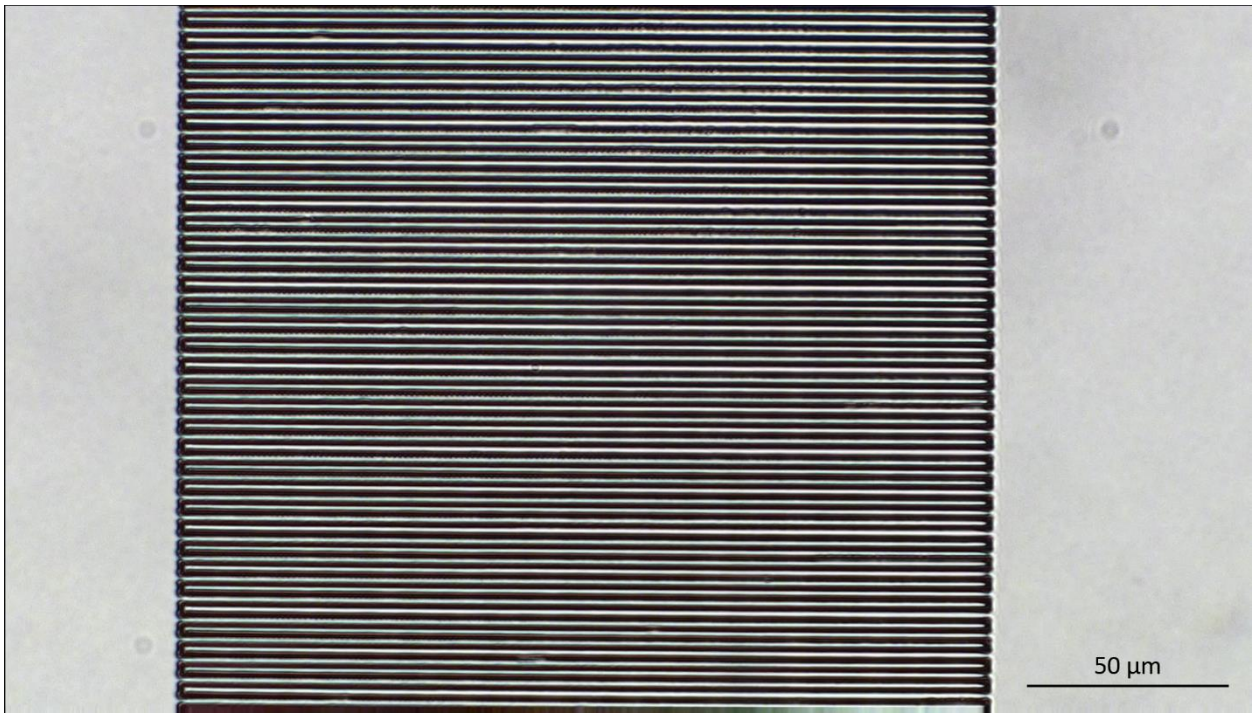

Figure S4. Pt micro-printed lines with reduced spacing. Each line is ~1.5 microns wide with a spacing of ~1 micron. Parameters used: stage velocity of 60 µm/s and laser power of 5mW.

Micro-printing of an Au/silicon-oxide/Pt junction

Au precursor solution was prepared by mixing 400 µl of a 0.125 M NaOH aqueous solution with 100 µl of 0.1 M $HAuCl_4$ aqueous solution. Deposition of the bottom metal Au layers was performed using laser power of 54 mW, stage velocity of 60 µm/s with laser modulation of 3 kHz. Silicon oxide and Pt layers were micro-printed with the same parameters reported in the experimental section. I-V measurements (**Figure S5b**) indicate conductance of Pt and Au lines while high resistivity of the silicon oxide layer is maintained.

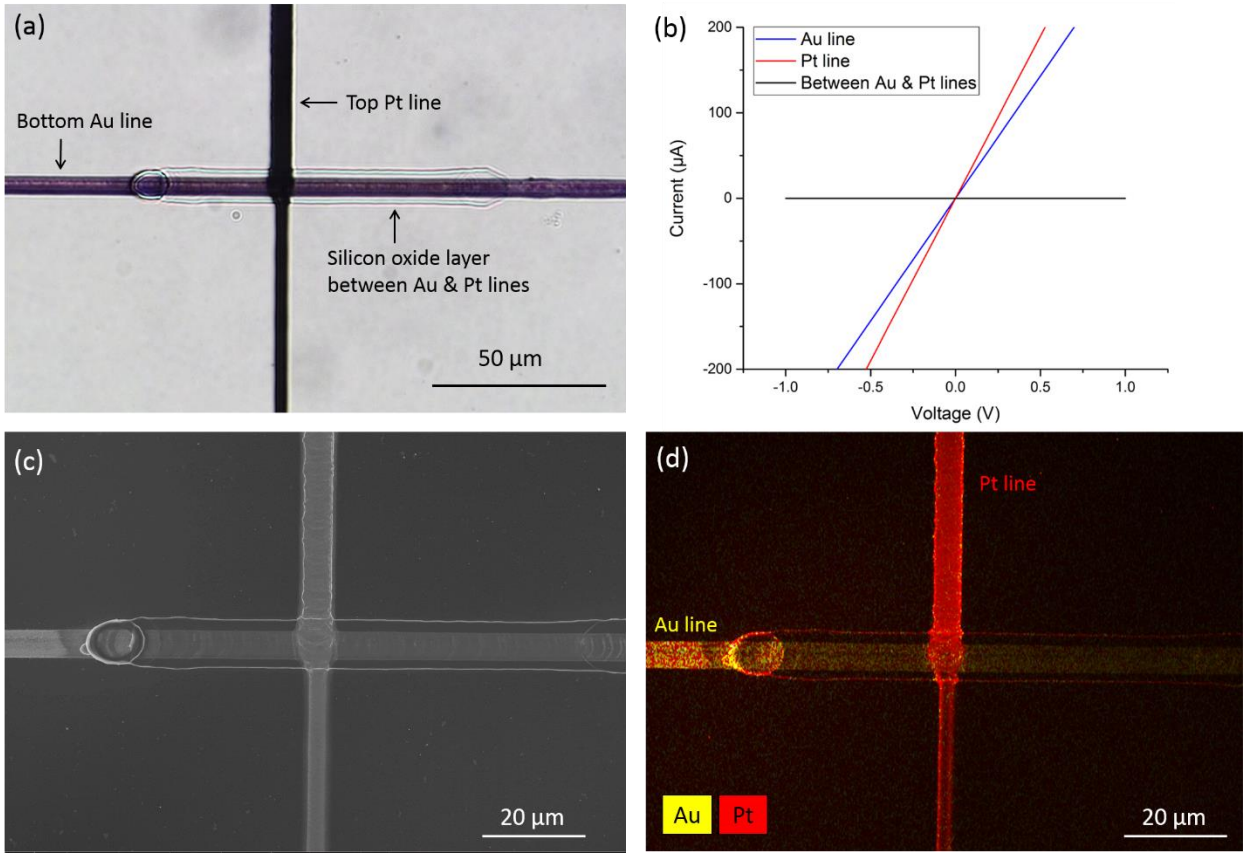

Figure S5. (a) Bright-field microscopy image and (b) corresponding I-V measurements of an Au/silicon-oxide/Pt junction. (c) HR-SEM image and (d) EDS mapping of Au and Pt.

Video SV1: shows the fabrication of a conducting/insulating/conducting multi-layered micro-structure using 3 wt% of Pt based precursor for the two conducting layers and TEOS based precursor for the insulating layer. The laser power was 14 mW, and the stage velocity was 100 and 400 μm/s for Pt and silicon oxide deposition, respectively.

Video SV2: demonstrates micro-printing in a microfluidic channel. Switching of precursors (Pt and TEOS based) was obtained by a microfluidic pressure-based controller. At the end of this video, a HR-SEM image of the fabricated cross-sectioned micro-structure is displayed.